

## Wave propagation near a fluid-solid interface: A spectral-element approach

Dimitri Komatitsch\*, Christophe Barnes<sup>†</sup>, and Jeroen Tromp\*

### ABSTRACT

We introduce a spectral-element method for modeling wave propagation in media with both fluid (acoustic) and solid (elastic) regions, as for instance in offshore seismic experiments. The problem is formulated in terms of displacement in elastic regions and a velocity potential in acoustic regions. Matching between domains is implemented based upon an interface integral in the framework of an explicit prediction-multicorrection staggered time scheme. The formulation results in a mass matrix that is diagonal by construction. The scheme exhibits high accuracy for a 2-D test case with known analytical solution. The method is robust in the case of strong topography at the fluid-solid interface and is a good alternative to classical techniques, such as finite differencing.

### INTRODUCTION

In the context of seismic exploration, numerical modeling of wave propagation has become an important research area, mainly because of the increasing geological complexity of regions in which seismic acquisition experiments are conducted. The finite difference method is commonly employed for this purpose. Unfortunately, the correct implementation of physical matching conditions at geological interfaces leads to significant numerical difficulties, for example, modeling surface topography, dipping or curved interfaces, and surface or interface waves (e.g., Robertsson, 1996). The spectral-element method (SEM) has been shown to be an efficient alternative tool for modeling wave propagation in complex structures, in particular in terms of accuracy, computational efficiency, and suitability to parallel computation (Seriani et al., 1992; Priolo et al., 1994; Casadei and Gabellini, 1997; Faccioli et al., 1997; Komatitsch, 1997; Komatitsch and Vilotte, 1998; Seriani, 1998; Komatitsch and Tromp, 1999).

In marine seismic experiments, one needs to model wave propagation in the acoustic part of the model (i.e., the water layer) as well as in the underlying solid. In a classical SEM formulated in terms of displacement (e.g., Komatitsch and Vilotte, 1998), continuity of displacement and velocity is enforced everywhere within the model. In the case of a boundary between an inviscid fluid and a solid, however, the kinematic boundary condition is perfect slip; therefore, only the normal component of velocity needs to be continuous across the interface, and thus the classical SEM method does not satisfy the correct interface condition. Furthermore, using displacement in the fluid introduces numerical artefacts associated with parasitic modes (Kiefling and Feng, 1976; Hamdi et al., 1978). To overcome these problems in the context of finite-element methods (FEM), alternative formulations have been introduced, for instance using displacement in the solid and pressure in the fluid (Craggs, 1971; Zienkiewicz and Bettess, 1978), which has the additional advantage of reducing the number of unknowns in the fluid, or using nonstandard finite elements (Bermudez et al., 1999). In the case of a fluid with homogeneous density in the rest state, it has also been noted in FEM that it is numerically more efficient to use a velocity potential rather than pressure in the fluid, because in the former approach, the resulting discrete system is symmetric and has a block-diagonal mass matrix (Thompson, 1994).

We show here how this velocity potential formulation can also be used in the context of a SEM and results in an accurate and robust scheme even in the case of a distorted fluid-solid interface. The discretization results in a global mass matrix that is exactly diagonal by construction. This constitutes a very significant advantage over classical FEMs, and over variants of the SEM based on a Chebyshev formulation, such as that of Seriani et al. (1992) and of Priolo et al. (1994). Moreover, we show that the equations can be integrated in time using a simple explicit predictor-multicorrector staggered time scheme. With such a diagonal mass matrix, and such a simple explicit time scheme, no inversion of a linear system is needed, and therefore big models can be dealt with easily, and a very

Published on Geophysics Online November 17, 1999. Manuscript received by the Editor January 25, 1999; revised manuscript received September 15, 1999.

\*Harvard University, Department of Earth and Planetary Sciences, Hoffman Bldg., 20 Oxford Street, Cambridge, Massachusetts 02138. E-mail: komatits@seismology.harvard.edu. E-mail: tromp@seismology.harvard.edu.

<sup>†</sup>Institut de Physique du Globe de Paris, Laboratoire de Sismologie, 4, place Jussieu, F-75252 Paris Cedex 05, France. E-mail: barnes@ipgg.jussieu.fr.

© 2000 Society of Exploration Geophysicists. All rights reserved.

efficient implementation can be obtained on parallel computers. This had already been shown for the purely elastic 3-D case by Komatitsch and Vilotte (1998) and Komatitsch and Tromp (1999). Although the tests presented here are 2-D, the formulation itself and the related algorithm are identical in 3-D.

### FORMULATION OF THE PROBLEM

We consider a linear elastic rheology for the heterogeneous solid, while the fluid is assumed to be inviscid and of homogeneous density. We restrict ourselves to isotropic materials, although SEM can handle anisotropic materials accurately (Seriani et al., 1995; Komatitsch et al., 2000). In the heterogeneous, elastic region, the linear wave equation can be written in the strong form as

$$\begin{aligned}\rho \ddot{\mathbf{u}} &= \nabla \cdot \boldsymbol{\sigma} + \mathbf{f}, \\ \boldsymbol{\sigma} &= \mathbf{C} : \boldsymbol{\varepsilon} = \lambda \operatorname{tr}(\boldsymbol{\varepsilon}) \mathbf{I} + 2\mu \boldsymbol{\varepsilon}, \\ \boldsymbol{\varepsilon} &= \frac{1}{2} [\nabla \mathbf{u} + (\nabla \mathbf{u})^T],\end{aligned}\quad (1)$$

where  $\mathbf{u}$  denotes the displacement vector,  $\boldsymbol{\sigma}$  the symmetric, second-order stress tensor,  $\boldsymbol{\varepsilon}$  the symmetric, second-order strain tensor,  $\mathbf{C}$  the fourth-order stiffness tensor,  $\lambda$  and  $\mu$  the two Lamé parameters,  $\rho$  the density, and  $\mathbf{f}$  an external force. The trace of the strain tensor is denoted by  $\operatorname{tr}(\boldsymbol{\varepsilon})$ ,  $\mathbf{I}$  denotes the identity tensor, the tensor product is denoted by a colon, and a superscript  $T$  denotes the transpose. A dot over a symbol indicates time differentiation.

The wavefield in the acoustic, inviscid fluid is governed by the conservation and dynamics equations which, neglecting the effects of gravity, are (e.g., Landau and Lifshitz, 1959):

$$\begin{aligned}\rho \dot{\mathbf{v}} + \nabla p &= \mathbf{0}, \\ \dot{p} + \rho c^2 \nabla \cdot \mathbf{v} &= 0,\end{aligned}\quad (2)$$

where  $\mathbf{v}$  denotes the velocity vector,  $p$  pressure, and  $c = \sqrt{\kappa/\rho}$  the speed of acoustic waves,  $\kappa$  being the bulk modulus of the fluid.

Assuming that the density  $\rho$  is homogeneous throughout the fluid, we have  $\nabla \times \mathbf{v} = \mathbf{0}$ , that is, the acoustic fluid is irrotational (Landau and Lifshitz, 1959). Thus the velocity  $\mathbf{v}$  can be written as the gradient of a scalar potential  $\phi$ . Substituting the definition  $\mathbf{v} = \nabla \phi$  in equation (2), we can eliminate pressure and obtain a second-order system that only involves the velocity potential:

$$\nabla^2 \phi = c^{-2} \ddot{\phi}.\quad (3)$$

Here  $\nabla^2$  is the Laplace operator.

To couple the two media at a fluid-solid interface, we have to ensure the continuity of traction  $\boldsymbol{\tau} = \boldsymbol{\sigma} \cdot \hat{\mathbf{n}}$ , where  $\hat{\mathbf{n}}$  denotes the unit normal to the interface. From equation (2) we see that the pressure  $p$  equals  $-\rho \dot{\phi}$ , which implies that the continuity of traction may be expressed as

$$\boldsymbol{\tau} = \rho \dot{\phi} \hat{\mathbf{n}}.\quad (4)$$

The kinematic boundary condition of continuity of the normal component of velocity is

$$\hat{\mathbf{n}} \cdot \nabla \phi = \hat{\mathbf{n}} \cdot \dot{\mathbf{u}}.\quad (5)$$

The free surface boundary condition is easily implemented in a weak formulation since the integral of traction along the boundary simply vanishes (e.g., Komatitsch and Vilotte, 1998).

On the remaining, artificial boundaries, outgoing waves need to be absorbed. In the elastic solid, this absorbing boundary condition may be approximated by dampers, that is, by relating the traction to velocity (Clayton and Engquist, 1977; Komatitsch and Vilotte, 1998):

$$\boldsymbol{\tau} = c_p \rho \mathbf{v}_n + c_s \rho \mathbf{v}_t,\quad (6)$$

where  $c_p = \sqrt{(\lambda + 2\mu)/\rho}$  denotes the  $P$ -wave speed,  $c_s = \sqrt{\mu/\rho}$  the  $S$ -wave speed, and  $\mathbf{v}_n$  and  $\mathbf{v}_t$  the normal and tangential components of velocity along the absorbing boundary. In the acoustic fluid, using a similar idea, the absorbing boundary condition may be approximated by a simple Sommerfeld-like condition (e.g., Thompson and Pinsky, 1996):

$$\hat{\mathbf{n}} \cdot \nabla \phi = -c^{-1} \dot{\phi}.\quad (7)$$

Note that the absorbing conditions (6) and (7) are only approximate, and small reflections from the artificial boundaries should be expected. In practice, the amplitude of these reflections is of the order of a few percents of the amplitude of the direct wave. Improved conditions can be used if needed (Quarteroni et al., 1998), but are less straightforward to implement. Note also that the absorbing boundary conditions are optimal for waves impinging with normal incidence and rapidly become less accurate when the angle of incidence differs from normal (Clayton and Engquist, 1977).

### DISCRETIZATION

We first rewrite the coupled system of equations (1)–(7) in a variational or weak form by dotting it with an arbitrary test vector  $\mathbf{w}$  in the solid, multiplying with an arbitrary test function  $w$  in the fluid, and integrating by parts over the region of interest (e.g., Thompson, 1994):

$$\begin{aligned}\int_{\Omega_s} \rho \mathbf{w} \cdot \ddot{\mathbf{u}} d\Omega + \int_{\Omega_s} \nabla \mathbf{w} : \mathbf{C} : \nabla \mathbf{u} d\Omega - \int_{\Gamma_i} \mathbf{w} \cdot \boldsymbol{\tau} d\Gamma \\ - \int_{\Gamma_{\text{abs}}^s} \mathbf{w} \cdot \boldsymbol{\tau} d\Gamma = \mathbf{0},\end{aligned}\quad (8)$$

$$\begin{aligned}\int_{\Omega_f} c^{-2} w \ddot{\phi} d\Omega + \int_{\Omega_f} \nabla w \cdot \nabla \phi d\Omega + \int_{\Gamma_i} w (\hat{\mathbf{n}} \cdot \nabla \phi) d\Gamma \\ + \int_{\Gamma_{\text{abs}}^f} c^{-1} w \dot{\phi} d\Gamma = \int_{\Omega_f} w f d\Omega.\end{aligned}\quad (9)$$

The solid and fluid regions of the model are denoted by  $\Omega_s$  and  $\Omega_f$ , respectively,  $\Gamma_{\text{abs}}^f$  denotes the acoustic absorbing boundary,  $\Gamma_{\text{abs}}^s$  denotes the elastic absorbing boundary, and  $\Gamma_i$  denotes the interface between the two media. The material parameters of the solid,  $\mathbf{C}$  and  $\rho$ , can be spatially heterogeneous. The source term  $f$  has been placed in the acoustic region; of course, it may also be placed in the solid. Imposing the continuity conditions (4) and (5) for the traction and for the normal velocity at the interface, we can rewrite the system (8)–(9) as

$$\int_{\Omega_s} \rho \mathbf{w} \cdot \ddot{\mathbf{u}} d\Omega + \int_{\Omega_s} \nabla \mathbf{w} : \mathbf{C} : \nabla \mathbf{u} d\Omega - \int_{\Gamma_i} \rho_0 \mathbf{w} \cdot \hat{\mathbf{n}} \dot{\phi} d\Gamma - \int_{\Gamma_{\text{abs}}^s} \mathbf{w} \cdot \boldsymbol{\tau} d\Gamma = \mathbf{0}, \quad (10)$$

$$\int_{\Omega_f} c^{-2} w \ddot{\phi} d\Omega + \int_{\Omega_f} \nabla w \cdot \nabla \phi d\Omega + \int_{\Gamma_i} w \dot{\mathbf{u}} \cdot \hat{\mathbf{n}} d\Gamma + \int_{\Gamma_{\text{abs}}^f} c^{-1} w \dot{\phi} d\Gamma = \int_{\Omega_f} w f d\Omega, \quad (11)$$

where  $\rho_0$  denotes the constant density of the fluid. This weak formulation forms the basis for the discretization of the problem in the next two sections.

### Spatial discretization

At this stage, we introduce a Legendre spectral element discretization of the variational problem (10)–(11). The domain  $\Omega$  is first meshed in terms of a set of  $n_{el}$  nonoverlapping elements  $\Omega_e$ , as in a classical FEM. Each of these elements is individually mapped to a reference domain  $\Lambda = [-1, 1]^{n_d}$  (a square in two dimensions,  $n_d = 2$ ; a cube in three dimensions,  $n_d = 3$ ) based upon an invertible local mapping  $\mathcal{F}_e : \Lambda \rightarrow \Omega_e$  such that  $\mathbf{x}(\boldsymbol{\xi}) = \mathcal{F}_e(\boldsymbol{\xi})$ . We make use of this mapping to go from the physical domain to the reference domain, and vice versa.

On the reference element  $\Lambda$ , we introduce a set of local basis functions consisting of polynomials of degree  $N$ . More precisely, we first map each element back to the reference domain  $\Lambda$  using the mapping  $\mathcal{F}_e$ . In each direction  $(\xi, \eta)$  of the reference element, we introduce a set of  $N + 1$  points  $\xi_i, i = 0, \dots, N, \in [-1, 1]$ , called the Gauss-Lobatto-Legendre (GLL) points, which are the roots of

$$(1 - \xi^2) P'_N(\xi) = 0, \quad (12)$$

where  $P'_N(\xi)$  is the derivative of the Legendre polynomial of degree  $N$ . These  $(N + 1)$  points can be computed by numerical resolution of equation (12) (Canuto et al., 1988, p. 61). We subsequently choose the set of basis functions to be products of the  $(N + 1)$  1-D Lagrange interpolants  $h_p(\xi), p = 0, \dots, N$ . By definition, these polynomials have the fundamental property that they vanish at all but one of the GLL points:

$$h_p(\xi_q) = \delta_{pq}. \quad (13)$$

Consequently, the piecewise-polynomial approximation of any given function  $u$ , in particular  $\mathbf{w}, \mathbf{u}, w$ , and  $\phi$ , can be written on the reference element as

$$u^e(\xi, \eta) = \sum_{p=0}^N \sum_{q=0}^N u^e(\xi_p, \eta_q) h_p(\xi) h_q(\eta). \quad (14)$$

To compute the gradient of a given function, we first differentiate equation (14) with respect to each variable:

$$\begin{aligned} \partial_{\xi} u^e(\xi, \eta) &= \sum_{p=0}^N \sum_{q=0}^N u^e(\xi_p, \eta_q) h'_p(\xi) h_q(\eta), \\ \partial_{\eta} u^e(\xi, \eta) &= \sum_{p=0}^N \sum_{q=0}^N u^e(\xi_p, \eta_q) h_p(\xi) h'_q(\eta), \end{aligned} \quad (15)$$

where  $h'$  denotes the derivative of the 1-D Lagrange interpolant. We then use the chain rule to obtain  $\partial_x = \xi_x \partial_{\xi} + \eta_x \partial_{\eta}$  and  $\partial_z = \xi_z \partial_{\xi} + \eta_z \partial_{\eta}$ . The components of the Jacobian matrix  $\xi_x, \xi_z, \eta_x$ , and  $\eta_z$  are computed by differentiating the mapping  $\mathcal{F}_e$ . Note that in practice the Jacobian matrix, which only describes the geometry of the problem, need not be calculated using polynomials of the same degree  $N$  as the interpolants, provided the shape of the elements is smooth enough; polynomials of degree 1 or 2 usually suffice for this purpose. The mapping is therefore often referred to as “subparametric” in the literature.

All the integrals appearing in equations (10)–(11) may now be approximated at the element level using the GLL integration rule:

$$\begin{aligned} \int_{\Omega} u w d\Omega &= \sum_{e=1}^{n_{el}} \int_{\Omega_e} u^e w^e d\Omega \simeq \sum_{e=1}^{n_{el}} \sum_{i=0}^N \omega_i \\ &\times \sum_{j=0}^N \omega_j J_e(\xi_i, \eta_j) u^e(\xi_i, \eta_j) w^e(\xi_i, \eta_j), \end{aligned} \quad (16)$$

where  $\omega_i > 0$  are the weights of the classical GLL integration rule, that are independent of the element and that can be computed numerically (Canuto et al., 1988, p. 61), and  $J_e$  is the Jacobian associated with the mapping  $\mathcal{F}_e$  from the element  $\Omega_e$  to the reference square  $\Lambda$ . Note that equation (16) involves a polynomial of degree  $2N$ , since it is the product of two polynomials of degree  $N$ , and that the GLL integration rule with  $N + 1$  points is exact only for polynomials of degree  $\leq 2N - 1$ . Therefore the integration is never exact, even in the case of simple rectangular (i.e., nondeformed) elements with a constant Jacobian. This choice of subintegration might seem surprising, but it is justified by the huge advantage of resulting in a diagonal mass matrix, and thus in a drastic reduction of the complexity of the algorithm and of the related CPU time (e.g., Komatitsch and Vilotte, 1998). This is the main difference between the SEM presented here and more classical FEM or SEM based on Chebyshev formulations, such as that of Seriani et al. (1992) and Priolo et al. (1994).

Let  $\mathbf{w}_N = (w_x, w_z)^T$ ,  $w_N, \mathbf{u}_N = (u_x, u_z)^T$ , and  $\phi_N$  denote the piecewise-polynomial approximations of the test functions for the solid, the test function for the fluid, the displacement in the solid, and the velocity potential in the fluid, respectively. Making use of equations (10) and (11), and multiplying equation (11) by the density of the fluid  $\rho_0$ , the discrete variational problem to be solved can thus be expressed as follows: For all time  $t$ , find  $\mathbf{u}_N$  and  $\phi_N$  such that for all  $\mathbf{w}_N$  and  $w_N$  we have

$$\begin{aligned} \langle \mathbf{w}_N, \rho \ddot{\mathbf{u}}_N \rangle + a_s(\mathbf{w}_N, \mathbf{u}_N) - A_s(\mathbf{w}_N, \phi_N)_{\Gamma_i} &= \langle \mathbf{w}_N, \boldsymbol{\tau}_N \rangle_{\Gamma_{\text{abs}}^s}, \\ \left\langle w_N, \frac{\rho_0}{c^2} \ddot{\phi}_N \right\rangle + a_f(w_N, \phi_N) + A_f(w_N, \mathbf{u}_N)_{\Gamma_i} \\ &= - \left\langle w_N, \frac{\rho_0}{c} \dot{\phi}_N \right\rangle_{\Gamma_{\text{abs}}^f} + \langle w_N, \rho_0 f_N \rangle. \end{aligned} \quad (17)$$

Discrete expressions for all the terms in equation (17) are given in Appendix A.

### Temporal discretization

After the spatial discretization in terms of spectral elements, imposing that equation (17) holds for any test functions  $(\mathbf{w}_N, w_N)$ , we are led, as in a classical FEM, to solve a coupled system of ordinary differential equations in time. Let  $U$  and  $\Phi$  denote the global vectors of unknown displacement in the solid and velocity potential in the fluid, respectively. We can rewrite the system (17) in matrix form as:

$$\begin{bmatrix} M_s & 0 \\ 0 & -M_f \end{bmatrix} \begin{pmatrix} \dot{U} \\ \dot{\Phi} \end{pmatrix} + \begin{bmatrix} D_s & A \\ A^T & D_f \end{bmatrix} \begin{pmatrix} U \\ \Phi \end{pmatrix} + \begin{bmatrix} K_s & 0 \\ 0 & -K_f \end{bmatrix} \begin{pmatrix} U \\ \Phi \end{pmatrix} = \begin{pmatrix} 0 \\ F \end{pmatrix}, \quad (18)$$

where  $M_s$  and  $M_f$  are the mass matrices in the solid and fluid, respectively,  $A$  is a coupling matrix between the two media,  $D_s$  is a matrix resulting from the absorbing condition on the boundary of the solid region,  $D_f$  is a matrix resulting from the absorbing condition on the boundary of the fluid region,  $F$  is the source term in the fluid, and  $K_s$  and  $K_f$  are the stiffness matrices in the solid and in the fluid, respectively. For detailed expression of these matrices obtained from equations (A.1)–(A.3) in Appendix A, see Thompson (1994). Note that  $A$  is very sparse because it represents the coupling between elements situated on both sides of the fluid-solid interface, and therefore it is nonzero for these coupled degrees of freedom only.

As mentioned above, one should note that a desirable property of the SEM, which results in a very significant reduction in the complexity and in the cost of the resolution algorithm, is the fact that the mass matrices  $M_s$  and  $M_f$  in equation (18) are diagonal by construction. This results from the use of Lagrange interpolants (14) at the GLL points in conjunction with GLL quadrature (16) (e.g., Komatitsch and Vilotte, 1998). This is also the reason why the velocity-potential formulation has been preferred over the classical formulation in terms of pressure, because in the latter case the formulation does not have this desirable property since the mass matrix has an additional contribution from the coupling matrix  $A$  (Thompson, 1994).

Time discretization of the system of second-order ordinary differential equations (18) is achieved using an explicit Newmark scheme written in a prediction-multicorrection formulation (Hughes, 1987, chapter 9; Zienkiewicz and Taylor, 1989, chapter 11). For a general second-order system of the form

$$M\ddot{\mathbf{d}} + C\dot{\mathbf{d}} + K\mathbf{d} = F, \quad (19)$$

the classical explicit Newmark scheme is written as

$$M\ddot{\mathbf{d}}_{n+1} + C\dot{\mathbf{d}}_{n+1} + K\mathbf{d}_{n+1} = F_{n+1}, \quad (20)$$

where

$$\mathbf{d}_{n+1} = \mathbf{d}_n + \Delta t \dot{\mathbf{d}}_n + \frac{\Delta t^2}{2} \ddot{\mathbf{d}}_n, \quad (21)$$

and

$$\dot{\mathbf{d}}_{n+1} = \dot{\mathbf{d}}_n + \Delta t[(1 - \gamma)\ddot{\mathbf{d}}_n + \gamma\ddot{\mathbf{d}}_{n+1}]. \quad (22)$$

It is conditionally stable, and it can be shown (e.g., Hughes, 1987) that it is second-order accurate if and only if  $\gamma = 0.5$ , which is the value that we use in this article. At the initial time

$t = 0$ , zero initial conditions are assumed (i.e.,  $\mathbf{d} = \mathbf{0}$  and  $\dot{\mathbf{d}} = \mathbf{0}$ ). Let us mention here that in a SEM, since the spatial discretization is based on high-degree polynomials, and therefore very accurate, it could be of interest to use more accurate (higher order) time schemes if needed, as proposed for instance by Tarnow and Simo (1994).

To take full advantage of the fact that the mass matrix  $M$  is diagonal, the scheme is implemented in practice in an equivalent iterative format based upon a staggered prediction/multicorrection technique. At each time step, we use an iterative scheme implemented as follows. We first compute predictors of the solution at the next time step in both domains. Then, we update the solution in one domain (either the fluid or the solid region) by solving the corresponding part of equation (18), using the predictors computed on the other side to evaluate the coupling term. We subsequently compute the solution in the other domain, this time using the updated solution in the first domain to evaluate the coupling term. We then iterate by returning to the first step, now using the updated solution. Such a scheme is classically called “staggered” in the literature. As mentioned above, since the mass matrix is diagonal, and since we use an explicit scheme, no inversion of a linear system is needed, as opposed to classical FEMs; therefore, the solver is very efficient, in particular on parallel computers.

The reader is referred to Park and Felippa (1980) for a study of staggered schemes, and to Hughes (1987) and Zienkiewicz and Taylor (1989) for a thorough study of the Newmark family of time schemes for hyperbolic problems, including a stability analysis and further details regarding the staggered prediction/multicorrection formulation.

### NUMERICAL TEST: FLAT INTERFACE

In order to validate the method, we consider two homogeneous half-spaces in contact at a flat interface, as shown in Figure 1. The lower part of the model is elastic, while the upper part is acoustic, a water layer. The material properties of the two layers are summarized in Table 1.

Poisson’s ratio  $\nu$  is chosen to be 0.25, therefore the  $S$ -wave speed in the elastic medium is related to the  $P$ -wave speed by  $c_S = c_P/\sqrt{3}$ . The size of each domain is  $6.4 \text{ km} \times 2.4 \text{ km}$ , which results in a global domain of  $6.4 \text{ km} \times 4.8 \text{ km}$ . The size of the spectral elements, shown by the mesh in Figure 1, is  $53.33 \text{ m} \times 53.33 \text{ m}$ . We use a total of  $120 \times 90 = 10\,800$  spectral elements. The polynomial degree is  $N = 5$ , therefore the total number of points of the global mesh is 271 051. Absorbing conditions are used on all the edges of the grid to simulate two half-spaces.

The source time function is a Ricker wavelet (i.e., the second derivative of a Gaussian). As with a polynomial degree  $N = 5$  the minimum number of points per wavelength required to obtain an accurate simulation is close to 5, we can select a

**Table 1. Material properties of the two homogeneous media (acoustic and elastic) used in both numerical experiments: the flat and the sinusoidal interfaces.**

	$c_P$ (m s <sup>-1</sup> )	$c_S$ (m s <sup>-1</sup> )	$\rho$ (kg m <sup>-3</sup> )
elastic	3400	1963	2500
acoustic	1500	—	1020

dominant frequency of 10 Hz for the source. The onset time is 115 ms. Since our goal is to validate the method, we need a very accurate time scheme in the tests involving a comparison to an analytical solution. Therefore, we use a small time step of  $\Delta t = 0.42$  ms in these first tests. In practice, the explicit Newmark scheme defined by equations (21)–(22) converges after two corrector iterations at each time step. The signal is propagated for 7150 time steps (i.e., 3 s).

**Source and receivers in the acoustic region**

In this first numerical experiment, both the source and the receivers are located in the acoustic region. The source is

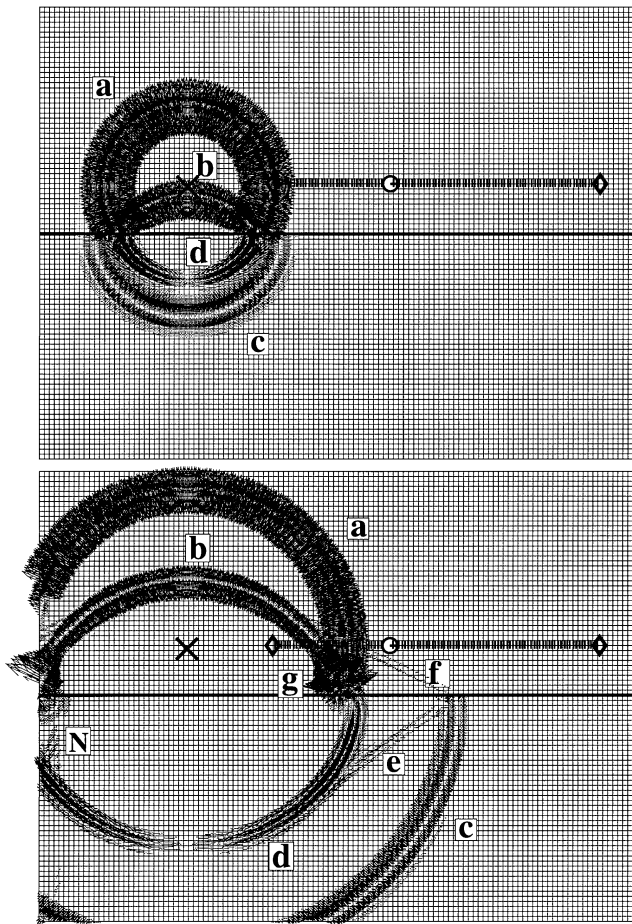


FIG. 1. Snapshots of the velocity vector at times  $t = 0.7$  s (top) and  $t = 1.26$  s (bottom) for the test case of a flat acoustic-elastic interface. The cells shown represent the mesh of spectral elements. The size of the domain is  $6.4 \text{ km} \times 4.8 \text{ km}$ , with the fluid-solid interface located at a depth of 2.4 km (thick black line). The cross indicates the position of the source, the dashed line between the diamonds indicates the position of the 110 receivers used to record the seismograms shown in Figure 2. The circle indicates the position of the receiver used for the comparison with the analytical solution presented in Figure 4. The direct (a) and reflected (b)  $P$ -waves can be observed in the fluid, the transmitted  $P$ - (c) and  $P$ -to- $S$  converted (d) waves are clearly visible in the solid. Significant refracted waves are also present, as can be seen on the second snapshot (e, f, g). On the left side of the second snapshot, small parasitic reflections from the sides, where approximate absorbing conditions are implemented, can also be observed (N).

placed at a distance of  $z_s = 500$  m above the interface. The 110 receivers are located on a horizontal line at a distance of  $z_r = 533.33$  m above the interface and at a horizontal offset from the source varying between 925 m and 4425 m.

Figure 1 shows the acquisition geometry and snapshots of the velocity vector field at times  $t = 0.7$  s and  $t = 1.26$  s. The corresponding seismograms for the two components of velocity are shown in Figure 2. Since the position of the receivers is chosen to coincide with grid points, which are not evenly spaced because they are based on the GLL points, the receivers are not exactly evenly spaced either. The time duration of the records is 3.0 s. Using these two representations, several phases can be distinguished (see Figure 3 for an illustration of the different phases that are present in the experiment): (a) the direct  $P$  wave, (b) the reflected  $P$  wave, (c) the transmitted  $P$  wave, (d) the  $P$ -to- $S$  converted wave, (e) the refracted  $P$ -wave converted to an  $S$ -wave in the solid, (f) the refracted  $P$ -wave in

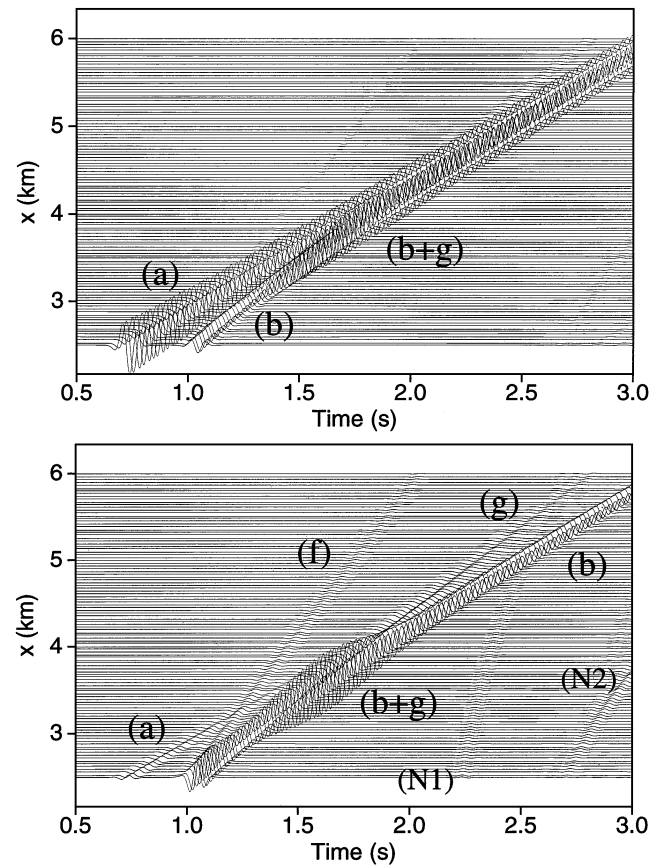


FIG. 2. Seismograms of the horizontal (top) and vertical (bottom) components of the velocity field recorded at the line of receivers shown in Figure 1. The direct  $P$ -wave (a) has a significant amplitude mainly on the horizontal component due to the geometry of the experiment. A strong refracted wave (g) appears on both seismograms for medium and large offsets. At medium offset, it is almost superimposed on the reflected  $P$ -wave (b) and has a comparable amplitude. Phase (g) separates at large offset, and is particularly clear on the vertical component between 2.0 and 2.8 s. The refracted  $P$ -wave (f), which is the first arrival at large offsets, has a smaller amplitude. Phases (N1) and (N2) are parasitic reflections due to the only approximate absorbing conditions implemented at the top and bottom boundaries.

the fluid, and (g) the refracted  $S$ -wave converted to a  $P$ -wave in the fluid.

In addition, spurious waves with small amplitude (N) are reflected from the absorbing boundaries, and can be clearly observed on the left of the second snapshot.

To further validate the method, we compare the numerical solution obtained with our SEM to the analytical solution of the problem. The analytical Green's function (Pilant, 1979) is convolved numerically with the source time function. Although this numerical convolution introduces some noise in the reference solution, it is negligible in practice. The comparison is performed at receiver 40, the receiver closest to the source being receiver 1. The two components of the numerical and analytical velocity are shown in Figure 4. The difference between the two curves is also shown in the same plot using an amplification factor of 5. The agreement is very good for all phases, which shows that the SEM is highly accurate both for direct and refracted phases. This further validates the coupling algorithm since refracted waves are particularly sensitive to the numerical accuracy of the coupling condition.

### Source and receivers in the elastic region

In order to determine the accuracy of the waves propagating in the solid, in particular the converted  $S$ -wave since it involves a conversion at the interface, we place the receivers in the elastic medium at a symmetric position on the other side of the interface. With this configuration we are able to test the ability of the SEM to correctly model converted phases. Because the analytical code we use to compute the reference solution needs both the source and the receiver to be located on the same side of the interface, we also place the source at a symmetric position below the interface. The recorded  $S$ -wave is a  $P$ -to- $S$  conversion reflected at the interface.

In Figure 5, we show the trace recorded at receiver 40 (solid line). The explosive source in the solid generates a direct

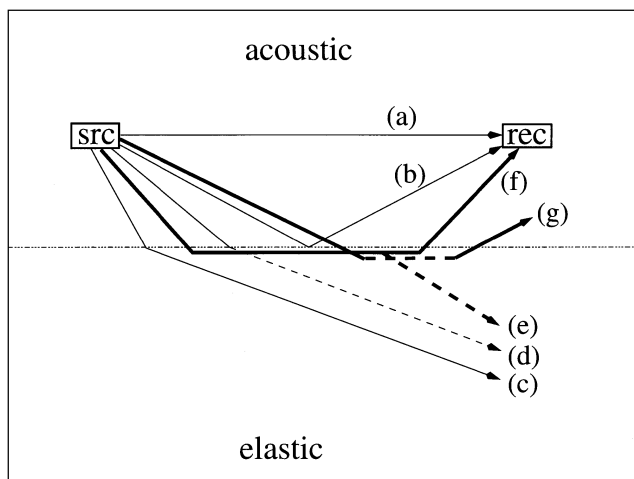


FIG. 3. Illustration of the main phases that are present in the first validation experiment with both the source and the receiver line located in the acoustic region. The solid lines represent  $P$ -wave rays, the dashed lines represent  $S$ -wave rays. The refracted rays are shown with thick lines. Phases (a)–(g) are labeled both on the snapshots in Figure 1 and on the seismograms in Figure 2.

$P$ -wave (a); in addition, the receiver records the reflected  $P$ -wave and the  $P$ -to- $S$  converted phases that are almost superimposed (b). The difference between the analytical and numerical solutions is very small, which shows in particular that the  $S$ -wave converted at the interface is modeled accurately. The difference is even smaller than in the previous test in the acoustic domain. This is due to the higher wave speed in the elastic region, which implies that the number of points per wavelength is higher.

### NUMERICAL TEST: SINUSOIDAL INTERFACE

In order to demonstrate the suitability of the method for models with bathymetry, we consider a model of the sea floor with strong sinusoidal topography, as shown in Figure 6. A free surface is implemented at the surface of the sea, an absorbing condition at the bottom of the solid, and periodic conditions on the vertical sides of the region of interest, in order to test the

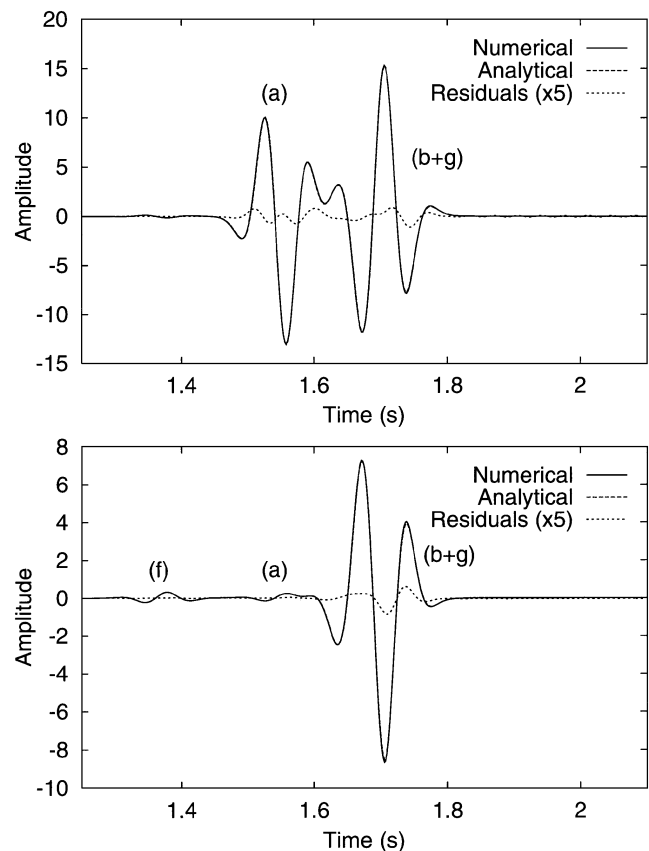


FIG. 4. Horizontal (top) and vertical (bottom) components of velocity recorded at receiver 40, whose exact location is indicated by a circle in Figure 1. The solid line represents the numerical solution, the dashed line, which is almost perfectly superimposed to the solid line, is the analytical solution, and the dotted line is the difference between the two curves amplified by a factor of 5. The agreement is excellent. Considering the position of the receiver, a very significant contribution from the second refracted wave (g) is recorded, around  $t = 1.65$  s, in addition to the direct  $P$ -wave (a), reflected  $P$ -wave (b), and first refracted  $P$ -wave (f). Since refracted waves are known to be very sensitive to the numerical accuracy of the matching condition between domains, this test demonstrates that it is accurately modeled.

behavior of different kinds of boundary conditions. Note that absorbing conditions could of course have been used instead of the periodic conditions on the vertical edges, as in the previous test. All model parameters remain the same as before. The source is located at  $x_s = 2908.33$  m at a depth of  $z_s = 1700$  m below the surface of the sea. The line of receivers is composed of 50 receivers going from  $x_{r1} = 3200$  m to  $x_{r50} = 5400$  m at a depth of  $z_r = 1500$  m. The horizontal mesh follows the shape of the sea floor in order to be able to impose the matching condition between domains at the sinusoidal interface. The length of the records is 2.1 s and the time step is  $\Delta t = 0.7$  ms; therefore the total number of time steps is 3000. The time step is chosen to be relatively small because of the fact that GLL points are clustered towards the edges of each spectral element, thereby creating small grid cells that reduce the value of the Courant stability condition of the explicit Newmark scheme. All other parameters remain the same as in the flat model simulation.

Snapshots of the velocity vector shown in Figure 6 illustrate the complexity of the wave field, in particular the presence

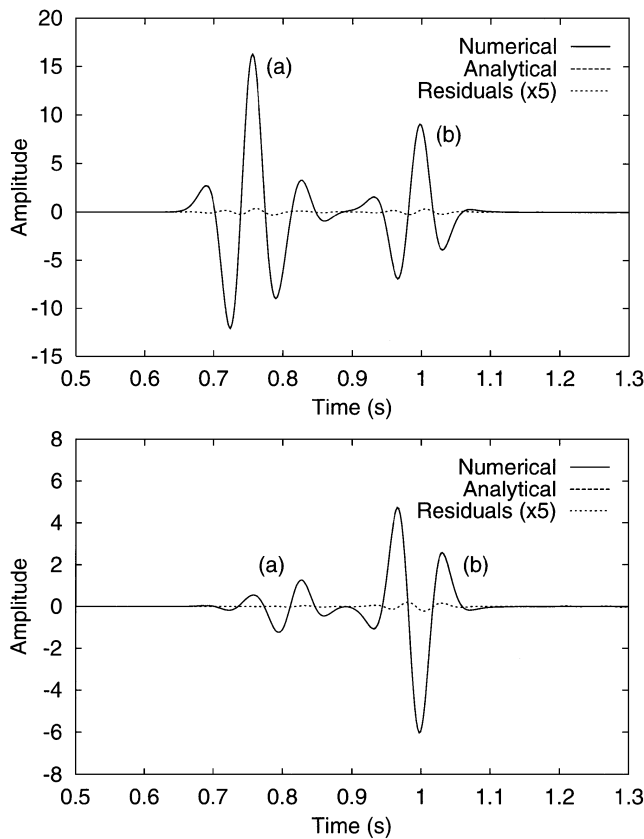


FIG. 5. Horizontal (top) and vertical (bottom) components of velocity recorded by a receiver located in the elastic medium, when an explosive source is placed in the same medium. The receiver records the direct  $P$ -wave (a) and a superposition of the reflected  $P$ -wave and  $P$ -to- $S$  converted waves (b). The dashed line, which is almost superimposed on the solid line, is the analytical solution, the dotted line is the difference between the two curves amplified by a factor of 5. These residuals are very small, which demonstrates the accuracy of the modeling technique, in particular for the  $S$ -wave converted and reflected at the interface.

of curved reflected and transmitted waves, triplications, and interface waves. Seismograms of the two components of velocity recorded at the line of receivers are shown in Figure 7. The main phases that can be distinguished are (a) the direct  $P$ -wave, (b) the strongly curved reflected  $P$ -wave on the first anticline on the right, (c) the  $P$ -wave reflected off the first anticline on the left [symmetric of phase (b)], (d) the  $P$ -wave reflected off the central syncline, which undergoes a time delay and therefore a triplication, (e) various transmitted  $P$ -waves, (f) various transmitted  $P$ -to- $S$  converted waves, (g) the  $P$ -wave reflected at the surface of the sea, and (h) a slow phase traveling along

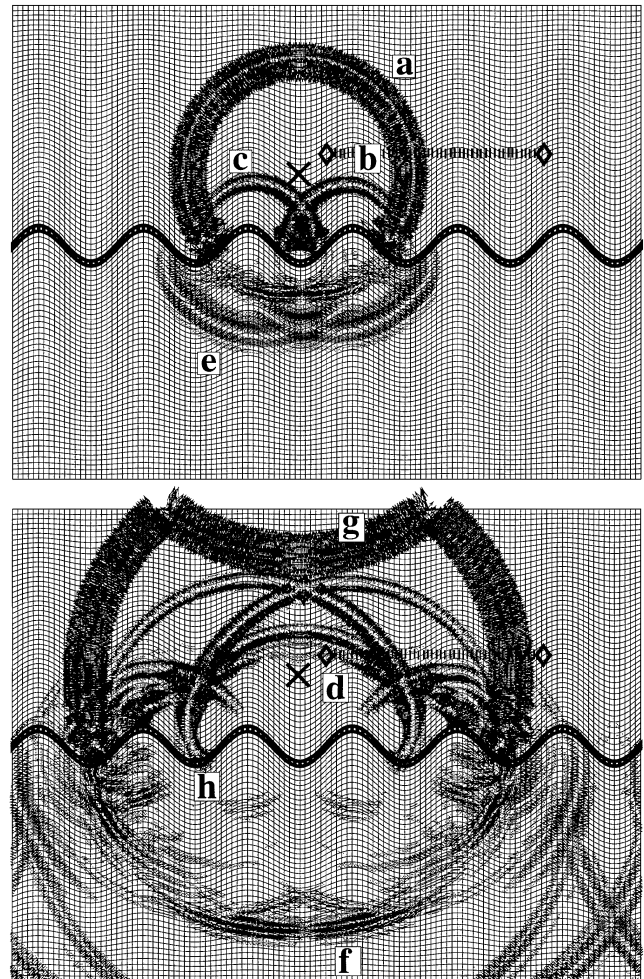


FIG. 6. Snapshots of the velocity vector at times  $t = 0.875$  s (top) and  $t = 1.575$  s (bottom) for a sea bottom with strong sinusoidal topography. The cross indicates the position of the source, and the dashed line between the diamonds is the line of receivers. Strongly curved reflected waves (b, c), triplications due to the topography of the sea floor (d), transmitted  $P$ -waves (e), and transmitted  $S$ -waves (f) can be observed. The direct  $P$ -wave (a) undergoes total reflection at the surface of the sea (g). The slow event traveling along the sea floor on the second snapshot (h) is interpreted to be a Stoneley wave. This slow event can be observed mainly on the second snapshot. On both vertical sides of the mesh, waves coming back from the other side of the mesh, due to the periodic conditions used in this simulation, can be observed.

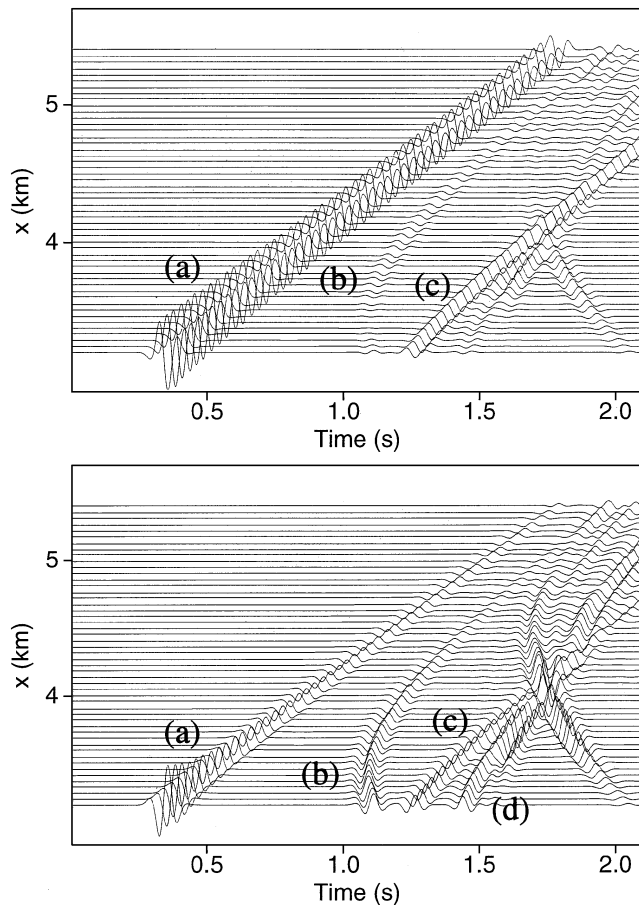


FIG. 7. Seismograms of the horizontal (top) and vertical (bottom) components of velocity recorded at the line of receivers shown in Figure 6 for the case of a sea floor with strong sinusoidal topography. In addition to the strong direct  $P$ -wave (a), the curved reflected phases (b) and (c) and the triplication (d) can be clearly observed.

the interface, which is interpreted to be a Stoneley wave (Biot, 1952).

### CONCLUSIONS

We have shown that the use of a velocity potential in homogeneous acoustic regions allows us to use the spectral element method for modeling wave propagation near a fluid-solid interface. Correct matching conditions between the fluid and the solid regions are enforced based upon a weak formulation of the interface equations. The discrete system obtained is solved in the context of an explicit prediction-multicorrection time scheme. With this choice of parameterization, the mass matrix is diagonal, unlike when pressure is used as the unknown within the fluid, and unlike when the variant of the spectral element method based on a Chebyshev formulation is used. In the case of a model with a flat interface, the agreement between the spectral element solution and the analytical solution is excellent. The method is also able to take into account models with strong topography at the fluid-solid interface. In that case, the wavefield is complex and includes numerous triplications and interface waves. Future work will focus on inhomogeneous fluids for which a scalar velocity potential cannot be defined.

### ACKNOWLEDGMENTS

The authors thank Emmanuel Chaljub, Jean-Pierre Vilotte, Anthony T. Patera, and Fabio Maggio for fruitful discussions. The comments of Johan Robertsson and of two anonymous reviewers helped improve the manuscript. The authors also gratefully acknowledge the support provided by DIA Consultants, and discussions with Terumitsu Tsuchiya. Partial support was also provided by UMR 7580 of the CNRS, by NSF and NEHRP, and by the David and Lucile Packard Foundation.

### REFERENCES

- Bermudez, A., Hervella-Nieto, L., and Rodriguez, R., 1999, Finite element computation of three-dimensional elastoacoustic vibrations: *J. Sound Vibr.*, **219**, 279–306.
- Biot, M. A., 1952, The interaction of Rayleigh and Stoneley waves in the ocean bottom: *Bull. Seis. Soc. Am.*, **42**, 81–93.
- Canuto, C., Hussaini, M. Y., Quarteroni, A., and Zang, T. A., 1988, *Spectral methods in fluid dynamics*: Springer-Verlag.
- Casadei, F., and Gabellini, E., 1997, Implementation of a 3D coupled Spectral Element solver for wave propagation and soil-structure interaction simulations: European Commission Joint Research Center Report EUR17730EN.
- Clayton, R., and Engquist, B., 1977, Absorbing boundary conditions for acoustic and elastic wave equations: *Bull. Seis. Soc. Am.*, **67**, 1529–1540.
- Craggs, A., 1971, The transient response of a coupled plate-acoustic system using plate and acoustic finite elements: *J. Sound Vib.*, **15**, 509–528.
- Faccioli, E., Maggio, F., Paolucci, R., and Quarteroni, A., 1997, 2D and 3D elastic wave propagation by a pseudo-spectral domain decomposition method: *J. Seismology*, **1**, 237–251.
- Hamdi, M. A., Ousset, Y., and Verchery, G., 1978, A displacement method for the analysis of vibrations of coupled fluid-structure systems: *Internat. J. Numer. Meth. Eng.*, **13**, 139–150.
- Hughes, T. J. R., 1987, *The finite element method, linear static and dynamic finite element analysis*: Prentice-Hall International.
- Kiefling, L., and Feng, G. C., 1976, Fluid-structure finite element vibrational analysis: *AIAA J.*, **14**, 199–203.
- Komatitsch, D., 1997, Méthodes spectrales et éléments spectraux pour l'équation de l'élastodynamique 2D et 3D en milieu hétérogène: Ph.D. thesis, Institut de Physique du Globe de Paris.
- Komatitsch, D., Barnes, C., and Tromp, J., 2000, Simulation of anisotropic wave propagation based upon a spectral element method, *Geophysics*, in press.
- Komatitsch, D., and Tromp, J., 1999, Introduction to the spectral element method for 3-D seismic wave propagation: *Geophys. J. Internat.*, **139**, 806–822.
- Komatitsch, D., and Vilotte, J. P., 1998, The Spectral element method: An efficient tool to simulate the seismic response of 2D and 3D geological structures: *Bull. Seis. Soc. Am.*, **88**, 368–392.
- Komatitsch, D., Vilotte, J. P., Vai, R., Castillo-Covarrubias, J. M., and Sánchez-Sesma, F. J., 1999, The spectral element method for elastic wave equations: Application to 2D and 3D seismic problems, *Internat. J. Numer. Meth. Eng.*, **45**, 1139–1164.
- Landau, L. D., and Lifshitz, E. M., 1959, *Fluid mechanics*: Pergamon Press.
- Park, K. C., and Felippa, C. A., 1980, Partitioned transient analysis procedures for coupled field problems: accuracy analysis: *J. Appl. Mech.*, **47**, 916–926.
- Pilant, W. L., 1979, *Elastic waves in the earth*: Elsevier Scientific Pub. Co.
- Priolo, E., Carcione, J. M., and Seriani, G., 1994, Numerical simulation of interface waves by high-order spectral modeling techniques: *J. Acoust. Soc. Am.*, **95**, 681–693.
- Quarteroni, A., Tagliani, A., and Zampieri, E., 1998, Generalized Galerkin approximations of elastic waves with absorbing boundary conditions: *Comp. Meth. Appl. Mech. Eng.*, **163**, 323–341.
- Robertsson, J. O. A., 1996, A numerical free-surface condition for elastic/viscoelastic finite-difference modeling in the presence of topography: *Geophysics*, **61**, 1921–1934.
- Seriani, G., 1998, 3-D large-scale wave propagation modeling by spectral element method on Cray T3E multiprocessor: *Comp. Meth. Appl. Mech. Eng.*, **164**, 235–247.
- Seriani, G., Priolo, E., Carcione, J. M., and Padovani, E., 1992, High-order spectral element method for elastic wave modeling: 62nd Ann. Internat. Mtg., Soc. Expl. Geophys., Expanded Abstracts, 1285–1288.

Seriani, G., Priolo, E., and Pregarz, A., 1995, Modelling waves in anisotropic media by a spectral element method, *in* Cohen, G., Ed., Third international conference on mathematical and numerical aspects of wave propagation: Soc. Ind. Appl. Math.

Tarnow, N., and Simo, J. C., 1994, How to render second-order accurate time-stepping algorithms fourth-order accurate while retaining the stability and conservation properties: *Comp. Meth. Appl. Mech. Eng.*, **115**, 233–252.

Thompson, L. L., 1994, Design and analysis of space-time and Galerkin-least-squares finite element methods for fluid-structure in-

teractions in exterior domains: Ph.D. thesis, Stanford Univ.

Thompson, L. L., and Pinsky, P., 1996, A space-time finite element method for structural acoustics in infinite domains. Part 1: Formulation, stability and convergence: *Comp. Meth. Appl. Mech. Eng.*, **132**, 195–227.

Zienkiewicz, O. C., and Bettess, P., 1978, Fluid-structure dynamic interaction and wave forces, an introduction to numerical treatment: *Internat. J. Numer. Meth. Eng.*, **13**, 1–16.

Zienkiewicz, O. C., and Taylor, R. L., 1989, The finite element method: V.2, Solid and fluid mechanics, 4th ed.: McGraw-Hill.

## APPENDIX A

### DISCRETE WEAK FORMULATION

In this appendix, we present expressions for the terms appearing in the discrete weak formulation (17) of the fluid-solid coupled system of equations (10)–(11), after having multiplied equation (11) by the density of the fluid  $\rho_0$ . The volume terms in the solid and in the fluid are

$$\begin{aligned} \langle \mathbf{w}_N, \rho \ddot{\mathbf{u}}_N \rangle &\simeq \sum_{\text{es}} \sum_{i=0}^N \omega_i \sum_{j=0}^N \rho_e^{ij} \mathbf{w}_{e,N}^{ij} \cdot \ddot{\mathbf{u}}_{e,N}^{ij} J_e^{ij} \omega_j, \\ a_s(\mathbf{w}_N, \mathbf{u}_N) &\simeq \sum_{\text{es}} \sum_{i=0}^N \omega_i \sum_{j=0}^N \nabla \mathbf{w}_{e,N}^{ij} : \mathbf{C}_e^{ij} : \nabla \mathbf{u}_{e,N}^{ij} J_e^{ij} \omega_j, \\ \left\langle w_N, \frac{\rho_0}{c^2} \ddot{\phi}_N \right\rangle &\simeq \sum_{\text{ef}} \sum_{i=0}^N \omega_i \sum_{j=0}^N \frac{\rho_0}{c^2} w_{e,N}^{ij} \ddot{\phi}_{e,N}^{ij} J_e^{ij} \omega_j, \\ a_f(w_N, \phi_N) &\simeq \sum_{\text{ef}} \sum_{i=0}^N \omega_i \sum_{j=0}^N \rho_0 \nabla w_{e,N}^{ij} \cdot \nabla \phi_{e,N}^{ij} J_e^{ij} \omega_j, \\ \langle w_N, \rho_0 f_N \rangle &\simeq \sum_{\text{ef}} \sum_{i=0}^N \omega_i \sum_{j=0}^N \rho_0 w_{e,N}^{ij} f_{e,N}^{ij} J_e^{ij} \omega_j. \end{aligned} \quad (\text{A-1})$$

The coupling terms between the fluid and the solid regions, which involve 1-D integration along the interface  $\Gamma_i$ ,  $\phi$  being known from the acoustic side and  $\mathbf{u}$  being known from the elastic side, are

$$\begin{aligned} A_s(\mathbf{w}_N, \phi_N)_{\Gamma_i} &\simeq \sum_{\text{eis}} \sum_{i=0}^N \rho_0 \mathbf{w}_{e,N}^{ij_0} \cdot \hat{\mathbf{n}}_e(\xi_i) \phi_{e,N}^{ij_0} J_e^{1D}(\xi_i) \omega_i, \\ A_f(w_N, \mathbf{u}_N)_{\Gamma_i} &\simeq \sum_{\text{eif}} \sum_{i=0}^N \rho_0 w_{e,N}^{ij_0} \dot{\mathbf{u}}_{e,N}^{ij_0} \cdot \hat{\mathbf{n}}_e(\xi_i) J_e^{1D}(\xi_i) \omega_i, \end{aligned} \quad (\text{A-2})$$

and the absorbing terms, which involve 1-D integration along the absorbing edges  $\Gamma_{\text{abs}}^s$  and  $\Gamma_{\text{abs}}^f$  in the fluid and solid regions are

$$\begin{aligned} \langle \mathbf{w}_N, \boldsymbol{\tau}_N \rangle_{\Gamma_{\text{abs}}^s} &\simeq \sum_{\text{eas}} \sum_{i=0}^N \mathbf{w}_{e,N}^{ij_0} \cdot \boldsymbol{\tau}_e^{ij_0} J_e^{1D}(\xi_i) \omega_i, \\ \left\langle w_N, \frac{\rho_0}{c} \phi_N \right\rangle_{\Gamma_{\text{abs}}^f} &\simeq \sum_{\text{eaf}} \sum_{i=0}^N \frac{\rho_0}{c} w_{e,N}^{ij_0} \phi_{e,N}^{ij_0} J_e^{1D}(\xi_i) \omega_i. \end{aligned} \quad (\text{A-3})$$

We have used the abbreviated notation  $\rho_e^{ij} = \rho_e(\xi_i, \eta_j)$ ,  $\mathbf{w}_{e,N}^{ij} = \mathbf{w}_{e,N}(\xi_i, \eta_j)$ , and so on in the above expressions. The sums  $\sum_{\text{es}}$ ,  $\sum_{\text{ef}}$ ,  $\sum_{\text{eis}}$ ,  $\sum_{\text{eif}}$ ,  $\sum_{\text{eas}}$ , and  $\sum_{\text{eaf}}$  correspond to sums over the elements in the elastic medium, fluid medium, along the coupling interface on the solid side, coupling interface on the fluid side, absorbing boundary in the solid, and absorbing boundary in the fluid, respectively. The 1-D Jacobian (i.e., the length element along the interface) is denoted by  $J_e^{1D}$ . These expressions are used in equation (17) to build the global linear system (18). The reader is referred to Komatitsch and Vilotte (1998) and Komatitsch et al. (2000) for further details regarding the spectral element formulation.